

Optical properties of superconducting pressurized LaH₁₀

S. F. Elatresh*

*Department of Physics, University of Guelph, Guelph, Ontario, Canada N1G 2W1 and
Department of Chemistry and Chemical Biology, Cornell University,
Baker Laboratory, Ithaca, New York 14853-1301, USA*

T. Timusk

Department of Physics and Astronomy, McMaster University, Hamilton, Ontario L8S 4M1, Canada

E. J. Nicol*

*Department of Physics, University of Guelph, Guelph, Ontario, Canada N1G 2W1
(Dated: February 24, 2022)*

Recently superconductivity has been discovered at around 200 K in a hydrogen sulfide system and around 260 K in a lanthanum hydride system, both under pressures of about 200 GPa. These record-breaking transition temperatures bring within reach the long-term goal of obtaining room temperature superconductivity. We have used first-principle calculations based on density functional theory (DFT) along with Migdal-Eliashberg theory to investigate the electron-phonon mechanism for superconductivity in the $Fm\bar{3}m$ phase proposed for the LaH₁₀ superconductor. We show that the very high transition temperature T_c results from a highly optimized electron-phonon interaction that favors coupling to high frequency hydrogen phonons. Various superconducting properties are calculated, such as the energy gap, the isotope effect, the specific heat jump at T_c , the thermodynamic critical field and the temperature-dependent penetration depth. However, our main emphasis is on the finite frequency optical properties, measurement of which may allow for an independent determination of T_c and also a confirmation of the mechanism for superconductivity.

I. INTRODUCTION

Neil Ashcroft proposed that hydrogen, upon becoming metallic at sufficiently high density, would transform to a superconductor at a critical transition temperature T_c possibly well above room temperature¹. This stimulated many scientists to search for superconductivity not only in pure hydrogen but also in hydrogen-rich compounds. The possible formation of metallic hydrogen has been reported at very high pressure by a number of groups²⁻⁵. Moreover, *ab-initio* crystal structure calculations have predicted high-temperature superconductivity in some hydrogen-rich compounds, some of which have been confirmed experimentally⁶⁻⁹.

Among a large number of possible hydrogen-rich compounds, several stoichiometries for the H-S system were identified as energetically competitive¹⁰ and experimentalists had been looking for superconductivity by compressing H₂S with H₂¹¹. H₂S is the only known stable compound in the system at ambient pressure and room temperature and its highest T_c was found to be 80 K at 160 GPa¹². In 2014, Duan *et al.*¹³ theoretically predicted that H₃S was a good candidate for superconductivity in the H-S system, with an expected T_c as high as 191-204 K at 200 GPa. This was followed by a remarkable discovery by Drozdov *et al.*¹⁴ who observed superconductivity at 203 K in H₂S compressed to 155 GPa (now identified as transforming to H₃S), which set the record for the highest T_c at the time. This subsequent experimental discovery helped to establish DFT calculations as having predictive power for finding new high temperature superconductors in the pressurized hydrides. Theoretic-

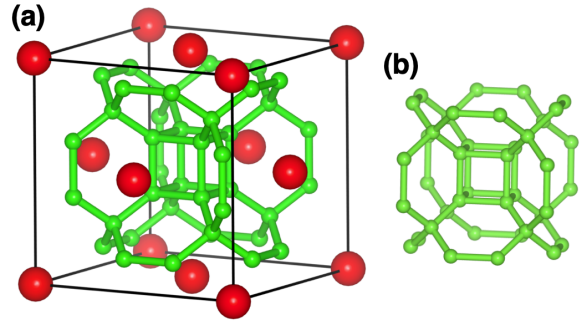


FIG. 1. (a) The conventional unit cell of the $Fm\bar{3}m$ crystal structure of LaH₁₀ where the red balls represent the La atoms in a fcc structure and the green balls are the hydrogen atoms. (b) The hydrogen atom arrangement shown separately.

cal structure calculations and experimental studies have since adopted several structures for H₃S, including the $R\bar{3}m$, $Im\bar{3}m$, and $Cccm$ phases^{10,13,15-21}, but the interpretation of X-ray data has favored the $Im\bar{3}m$ phase for the high pressures involved.

The record-breaking discovery of very high T_c in H₃S has encouraged further efforts in the search for room temperature superconductivity in pressurized hydride materials. Several superconducting hydride materials have been predicted, including MgH₆ with $T_c=271$ K at 300 GPa²², CaH₆ with $T_c=235$ K at 150 GPa²³, and YH₆ with $T_c=264$ K at 120 GPa²⁴. Interestingly, two independent first-principles structure search studies revealed some stable H-rich clathrate structures to be potential room-temperature superconductors^{25,26}. In par-

particular, the La-H and Y-H systems were theoretically investigated, and some compounds have been identified as good candidates for room-temperature superconductivity. From the Y-H system, the structures YH_4 , YH_6 , and YH_{10} were proposed^{24–26}. While from the La-H system several stable compounds were identified: LaH_3 , LaH_4 , LaH_5 , LaH_8 , and LaH_{10} . Most notably, YH_{10} and LaH_{10} were considered the most likely structures to exhibit possible room-temperature superconductivity, where the $T_c \sim 303$ K at 400 GPa²⁶ for YH_{10} and $T_c \sim 274$ –286 K at 210 GPa for the $Fm\bar{3}m$ phase proposed for the LaH_{10} . As a result, the La-H system became of interest, with studies proposing LaH_{10} to be thermodynamically stable above 150 GPa. Indeed, the lanthanum compound was synthesized²⁷ and two groups have reported near-to-room-temperature superconductivity with $T_c \sim 260$ K at 190 GPa²⁸ and $T_c \sim 250$ K at about 170 GPa²⁹. This is the highest T_c that has been reported to date. Various structures and compositions have been suggested for the superconducting La-H system including $P6/mmm$ for LaH_{16} ³⁰ and $R\bar{3}m$, $C2/m$, $Fm\bar{3}m$ for the LaH_{10} composition. However, recently Errea, *et al.*³¹ have shown that the Born-Oppenheimer energy surface with classical treatment displays many local minima and by including quantum effects all these phases collapse to a single phase, $Fm\bar{3}m$, which is highly symmetric.

In this work, we report results from first-principles calculations based on DFT and Migdal-Eliashberg theory, to evaluate T_c and other superconducting properties of LaH_{10} . In particular, we focus on studying the most promising candidate structure proposed for LaH_{10} , the $Fm\bar{3}m$ phase. We emphasize the finite frequency optical conductivity which is related to reflectance. The latter is a technique accessible to experiment in high pressure cells and has been used with success in H_3S ³². It can be used to identify important fundamental information about superconductivity such as the binding energy of electrons in the superconducting condensate and the mechanism for binding, which for conventional superconductors is the electron-phonon interaction. Moreover, it has been proposed that it can provide an independent measurement of T_c for the pressurized hydrides³³.

The structure of our paper is as follows. In Sec. II, we begin by calculating the electronic band structure and density of states, illustrating the Fermi surface. This is followed by a calculation of the phonon dispersion curves and the phonon density of states in the harmonic approximation. These are then used further to calculate the electron-phonon interaction shown in Sec. III. Proceeding to the calculation of superconducting properties in Sec. III, we calculate T_c , the functional derivative, the isotope effect, and the important BCS ratios for the energy gap, the specific heat jump at T_c and the thermodynamic critical field. We then proceed to the calculation of the temperature-dependent superfluid density (or inverse square of the penetration depth) followed by the finite frequency optical conductivity and reflectance. To examine the influence of anharmonicity on these prop-

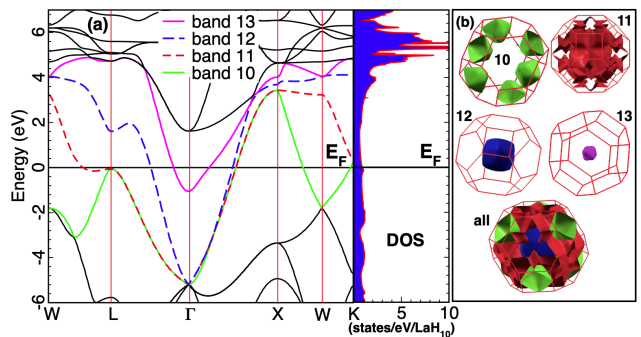


FIG. 2. Calculated electronic properties for LaH_{10} at 210 GPa: (a) the electronic band structure and the density of states (DOS) and (b) the Fermi surface. Each band crossing the Fermi level E_F in (a) is given a color which corresponds with the piece of Fermi surface with the same color in (b).

erties, we also provide comparison calculations based on an anharmonic spectrum taken from Errea *et al.*³¹. We provide our final summary in Sec. IV.

II. ELECTRONIC AND PHONONIC PROPERTIES

We begin by addressing the electronic and the phononic properties, as well as, the electron-phonon coupling. It has been suggested that the LaH_{10} $Fm\bar{3}m$ phase has a wide pressure range for dynamic stability, down to about 210 GPa for harmonic phonon calculations²⁵ and lower for anharmonic quantum calculations³¹, in the range where superconductivity has been observed. Consequently, we have calculated the electronic band structure and density of states for LaH_{10} at 210 GPa (Fig. 2(a)). Full structural optimization, electronic band structure, density of states, and Fermi surfaces calculations were performed within density-functional theory (DFT) using the ABINIT code³⁴ with 1 and 11-electron Hartwigsen-Goedecker-Hutter pseudopotential³⁵ for H and La, respectively, and the local density approximation (LDA) by Teter Pade parameterization³⁶. A plane-wave expansion with 50 Ha cut-off and a \mathbf{k} -point grid for self-consistent calculations as large $24 \times 24 \times 24$. These dense \mathbf{k} -point grids are sufficient to ensure convergence for enthalpies to better than 1 meV/atom. The symmetry information of the LaH_{10} $Fm\bar{3}m$ phase and the calculated X-ray diffraction obtained after performing full structural optimization at 210 GPa can be found in Table S1 and Fig. S1³⁷, respectively. The electronic band structure indicates that LaH_{10} at 210 GPa is a good metal, which is consistent with previous calculations reported at 300 GPa²⁵. As was expected, the partial electronic density of states (Fig. S2³⁷) indicates that the La contribution is greater than H. There are four bands crossing the Fermi level and the Fermi surface is shown in Fig. 2(b) in colors which correspond to each of the four bands. The Fermi surfaces of bands 10, 12, and

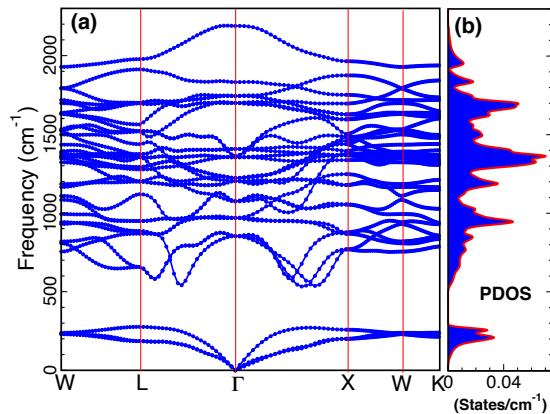


FIG. 3. Calculated phonon properties for LaH₁₀ at 210 GPa: (a) the phonon dispersion curves and (b) the phonon density of states (PDOS).

13 are quite simple while the Fermi surface of band 11 is quite complicated. Similar pictures are also found in Ref.³⁸ which discusses the possibility of multiband superconductivity associated with different Fermi surfaces.

The density of states at the Fermi level, $N(E_F)$, has a large number of states, 11.85 states/Ry, which is larger by factors of 1.18 and 1.58 than fcc LaH₁₀ and H₃S reported at 300 GPa²⁵ and 200 GPa¹⁷, respectively. This variation with pressure is consistent with the recent finding by Errea et al.³¹ that the density of states at the Fermi level decreases with increasing pressure. A close up view of our calculation of the electronic density of states near the Fermi level (Fig. S3³⁷) shows a peak in the density of states just below E_F , which likely has its primary origin in the flattening of band 11 near the L point. A large density of states at the Fermi level is favorable for superconductivity.

Now we discuss the phonon characteristics, as they play an important role in electron-phonon mediated superconductivity. We have performed phonon calculations for the $Fm\bar{3}m$ phase for LaH₁₀ at 210 GPa, in a pressure region where measurements confirm a very high T_c . The phonon and the electron-phonon coupling (EPC) calculations were performed with density-functional perturbation theory (DFPT)³⁹ and the harmonic approximation as implemented in ABINIT code³⁴ with the same parameters as in the DFT calculations. The dynamical matrices were calculated initially on uniform \mathbf{q} -point meshes, from which interatomic force constants are obtained and used to interpolate the phonon dispersions over the entire Brillouin zone. The phonon band structure and density of states for the \mathbf{q} -point grid was tested until convergence was achieved. It was found that a $6 \times 6 \times 6$ grid was required. The EPC implementation in the ABINIT code³⁴ is similar to that implemented by Liu and Quong⁴⁰ and Savrasov⁴¹.

The phonon band structure and density of states for the LaH₁₀- $Fm\bar{3}m$ phase is shown in Fig. 3 and they are

similar to previous calculations at 300 GPa²⁵ where GGA was used. This highlights that both GGA and LDA provide a consistent description of vibrational properties of the LaH₁₀- $Fm\bar{3}m$ phase. It is clear from this that the phonon frequencies have a weak dependence on increasing pressure, which indirectly might imply a weak dependence of T_c on pressure^{29,31}. The highest phonon frequency for LaH₁₀ at 210 GPa is at ~ 2190 cm⁻¹ or ~ 272 meV (Fig. S4³⁷). The very lowest phonon branches result from the heavy mass lanthanum phonon modes and the rest of the dispersion curves at higher frequencies are due to the lighter mass hydrogen. The role of the lanthanum appears to be that of providing conduction electrons and also caging the hydrogen to provide a shorter H bond length than normal. The La-La bond length in the fcc structure underlying LaH₁₀ (Table S1, Figs. S5 and S6³⁷) is typical of ordinary pure metals at ambient pressure but the shortened distance between the hydrogen is not. Rather, the shortest H-H distance in LaH₁₀ at 210 GPa (Figs. S5 and S7³⁷) is 1.084 Å, which is more consistent with the prediction of Neil Ashcroft for metallic hydrogen at a pressure near 500 GPa¹. The shortest La-H distance is 2 Å (Fig. S8³⁷). As a result, the La cage might be viewed as assisting in shortening the H-H distance so that the 500 GPa needed for pure metallic hydrogen is now only of order 200 GPa for metallic behavior.

Finally, we note that our calculation of the harmonic phonon dispersion curves at 210 GPa does not show any unstable modes. Interestingly, Errea et al.³¹ have reported that unstable modes appear in the harmonic approximation at pressures below ~ 230 GPa and that including anharmonicity is required to stabilize this structure below 230 GPa. We have investigated this matter further. The pressure where the harmonic approximation breaks down may be varied depending on the choice of some DFT parameters, including the type of exchange-correlation and pseudopotential⁴². We have produced a result with unstable modes when we used harmonic calculation parameters similar to Ref.³¹. To examine the quality of the harmonic electron-phonon spectral function used in this work and the influence of anharmonicity, we have included comparison calculations, where an anharmonic electron-phonon spectrum from Errea et al.³¹ is used as input.

III. SUPERCONDUCTING PROPERTIES

We now continue on to the electron-phonon coupling and emphasize its contribution to superconducting properties. We have used our calculation of the electronic structure and phonon dispersion curves to calculate the electron-phonon spectral function $\alpha^2F(\omega)$ which enters the Migdal-Eliashberg theory of superconductivity and is the pairing “glue” for Cooper pairs in conventional superconductors⁴³. The $\alpha^2F(\omega)$ is shown in Fig. 4(a) where we see that it looks much like the phonon density of states

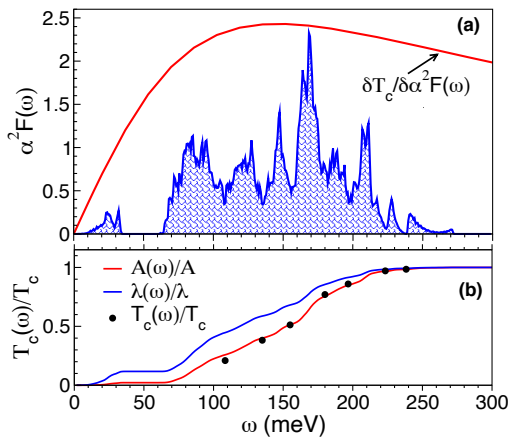


FIG. 4. (a) $\alpha^2 F(\omega)$ for the $Fm\bar{3}m$ phase of LaH_{10} at 210 GPa. Also, shown is the functional derivative $\delta T_c / \delta \alpha^2 F(\omega)$ as a function of energy ω which indicates which of these energies are more effective for raising T_c . This curve has been scaled up by a factor of 15. (b) $T_c(\omega)/T_c$ versus ω as well as electron-phonon renormalization parameter $\lambda(\omega)/\lambda$ and area $A(\omega)/A$.

from Fig. 3(b) but with modified strength as a function of energy due the variation of the electron-phonon coupling vertex.

In the following, this $\alpha^2 F(\omega)$ was used in our calculations of superconducting properties which are based on numerical iteration of the nonlinear coupled Migdal-Eliashberg equations for the real-frequency complex gap function $\Delta(\omega, T)$ and complex renormalization function $Z(\omega, T)$.^{43–45} The linearized imaginary-frequency axis equations based on Matsubara frequencies ω_n were used to calculate T_c . Then the coupled nonlinear imaginary-axis equations were used to calculate thermodynamic properties for temperatures below T_c .^{43,44} An analytic continuation procedure was then used to evaluate the real frequency gap and renormalization functions from the imaginary axis solutions⁴⁶. The real frequency axis quantities then allowed for the energy gap and other transport properties to be obtained. The finite frequency conductivity was evaluated based on formulas in Ref.^{44,47} and the reflectance was calculated following the prescription given in Ref.³². The formalism is lengthy to write down and has been presented in the literature numerous times, consequently, for formulas and further descriptions see Refs.^{43–45}. We will emphasize results and discussion here.

A. The critical temperature

We begin by discussing the characteristics of this spectral function and the features which have an impact on increasing the T_c . Using the $\alpha^2 F(\omega)$ spectrum in the linearized form of the Migdal-Eliashberg equations on the imaginary frequency axis^{43,45} and iterating these equations, we may obtain T_c for a particular choice of

Coulomb pseudopotential parameter μ^* or, alternatively, we can fix the value of T_c and iterate for μ^* .⁴³ Historically, it has been typical to choose the μ^* to give the experimental T_c . Once μ^* is fixed, then all other superconducting properties follow with no free parameters. For a typical value of $\mu^* = 0.128$, we match the $T_c = 237.9$ K that is found for an anharmonic calculation of $\alpha^2 F(\omega)$ including quantum corrections at a similar pressure³¹ [designated as the Errea spectrum]. This is also close to the experimental T_c for this pressure. This allows us to make comparison with an alternative calculation of $\alpha^2 F(\omega)$ as we calculate the superconducting properties of LaH_{10} . Indeed, in Table 1, we list the comparison of results from our spectrum with those that we have calculated from the Errea spectrum.

TABLE I. Summary of quantities calculated using two independent $\alpha^2 F(\omega)$ spectra and fixing the $T_c = 237.9$ K.

	<i>Errea spectrum</i> (anharmonic) (214 GPa)	<i>Our spectrum</i> (harmonic) (210 GPa)
μ^*	0.15	0.13
λ	2.02	2.16
A (meV)	133	130
ω_{1n} (meV)	113	102
T_c/A	0.155	0.157
T_c/ω_{1n}	0.18	0.20
Isotope coeff. β	0.484	0.489
Δ_0 (meV)	49	51
$2\Delta_0/k_B T_c$	4.78	4.93
$\Delta C(T)/\gamma T_c$	2.97	2.91
$\gamma T_c^2/H_c^2(0)$	0.131	0.130

In Fig. 4(a), we show the functional derivative of T_c with respect to $\alpha^2 F(\omega)$, this quantity indicates which frequencies in the spectrum are more important for increasing T_c . While the curve is entirely positive, indicating that adding more weight in the spectrum at any frequency will increase T_c , it is clear that the broad maximum in this spectrum favors the region where we find the hydrogen phonons and that the low frequency La phonons have very little effect on the T_c , indeed our calculations show that they only contribute a few degrees to T_c . Consequently, the large T_c is due to the electrons coupling to hydrogen phonons, as expected from simple arguments that T_c should scale with phonon frequency. Similar results have been recently analyzed by others, for example Refs.^{48,49}.

Isotopic substitution is a classic experiment to confirm the electron-phonon interaction as the underlying mechanism for superconductivity. The isotope experiment, where the hydrogen is replaced with deuterium, was done and the T_c was found to be reduced²⁹. This can be viewed as a measurement of the total isotope effect, to good approximation, given that the La phonons play little role in T_c . If the La had been important, then the deuterium substitution could only be viewed as giving a partial isotope effect⁴³. Simple Bardeen-Cooper-Schrieffer (BCS) theory predicts $T_c \propto M^{-\beta}$, where M is the ion mass

for a monatomic crystal and the isotope effect coefficient $\beta = 0.5$. However, in Migdal-Eliashberg theory, which is the extension of BCS theory to include the details of the electron-phonon interaction, the isotope coefficient is more complex. It can be reduced significantly from 0.5 with finite μ^* and even be negative in value, as has been seen in experiments on conventional superconductors. For $\mu^* = 0$, $\beta = 0.5$ regardless the $\alpha^2F(\omega)$. Here, we have calculated the the total isotope effect coefficient to be 0.489 in Eliashberg theory using the functional derivative method of Rainer and Culetto⁵⁰. Our value is in reasonable agreement with experiment, which finds 0.46 at 150 GPa²⁹, and with other theoretical calculations showing the pressure dependence of the coefficient⁵¹. Our calculation includes the low frequency La-based phonons but even when we remove those phonons to do the partial isotope effect due to hydrogen only, the coefficient barely changes, as expected from the functional derivative.

In Fig. 4(b), we also show the $\lambda(\omega)$ curve commonly exhibited with $\alpha^2F(\omega)$ spectra in the literature. λ is the electron-phonon mass renormalization parameter and is calculated using $\lambda = 2 \int_0^\infty d\omega \alpha^2F(\omega)/\omega$. This parameter, which is 2.16 for our spectrum, is very important in the theory and is often taken as a measure of the electron-phonon interaction, appearing in simplified T_c equations, such as the McMillan equation⁵² or the Allen-Dynes equation⁵³. A more significant parameter for T_c is the area under the $\alpha^2F(\omega)$, $A = \int_0^\infty d\omega \alpha^2F(\omega)$. Shown here is the partial integration of λ as a function of energy ω , *i.e.*, $\lambda(\omega) = 2 \int_0^\omega d\Omega \alpha^2F(\Omega)/\Omega$, normalized to λ . In comparison, we show the integrated area of the $\alpha^2F(\omega)$

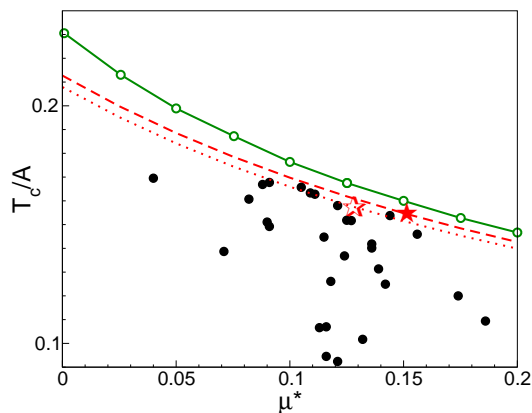


FIG. 5. T_c/A versus μ^* . The green curve with circles is the upper bound allowed by Migdal-Eliashberg theory. The black points are the data points for many conventional superconductors as tabulated in Ref. ⁴³ based on primarily $\alpha^2F(\omega)$ spectra measured in experiment via tunneling inversion. The red stars are the values for LaH₁₀ using the spectra discussed here. The dashed and dotted curves are calculated with these same two spectra (anharmonic and harmonic, respectively) fixing the area A and varying the μ^* . This plot demonstrates that the LaH₁₀ spectra are nearly optimal.

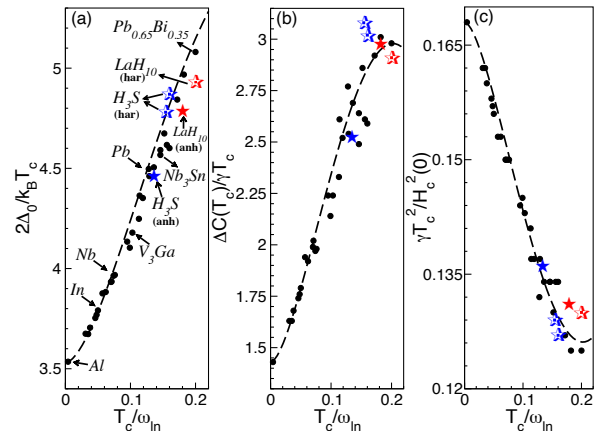


FIG. 6. The three main BCS ratios as modified by strong electron-phonon coupling measured by T_c/ω_{ln} : (a) $2\Delta_0/k_B T_c$, (b) $\Delta C(T_c)/\gamma T_c$, (c) $\gamma T_c/H_c^2(0)$. For $T_c/\omega_{\text{ln}} \rightarrow 0$, we recover the weak coupling BCS limit of 3.53, 1.43, and 0.168, respectively. The solid black points are the results for various conventional superconductors taken from Ref. ⁴³. The red stars are our calculations for LaH₁₀ and the blue stars are from previous calculations⁵⁶ for H₃S (open and filled stars for the harmonic and anharmonic spectra, respectively).

and the T_c values calculated using just the lower part of the spectrum up to that energy. One sees that the T_c tracks the area under $\alpha^2F(\omega)$ more closely than the λ . Indeed, it has been discussed in the past that there is an important relationship between the area and T_c with an upper bound on T_c/A provided by general Eliashberg theory^{54,55}. This is shown in Fig. 5 where the upper bound of T_c/A is plotted as a function of μ^* as the green curve with open circles⁵⁴. Shown are black points from the spectra and data of many conventional superconductors⁴³. These points always fall below the upper bound. The open and filled red stars are for our harmonic spectrum and the anharmonic Errea spectrum, respectively. The red curves are for the fixed $\alpha^2F(\omega)$ spectrum, where we vary μ^* and therefore the T_c (dashed and dotted curves for anharmonic and harmonic curves, respectively). It is clear that both spectra for LaH₁₀ are near the upper limit and this means that they are highly optimized in their electron-phonon interaction for the highest T_c possible given the repulsive Coulomb potential parameter μ^* . Similar results were found for pressurized H₃S⁵⁶. Recently, Quan *et al.*⁴⁸ have also analyzed results for various hydrides and find good agreement with the area correlating with T_c .

B. BCS ratios

Another important parameter defining the $\alpha^2F(\omega)$ spectrum is a particular moment of the spectrum called $\omega_{\text{ln}} = (2/\lambda) \int_0^\infty d\omega \alpha^2F(\omega) \ln(\omega)/\omega$ ⁵³. This is treated as a typical average phonon frequency, replacing the Debye

frequency. Over a number of years of intense study of the Eliashberg equations with both numerical and experimental data, the ratio T_c/ω_{ln} has been identified as one of the best measures of strong electron-phonon coupling in conventional superconductors and simple formulas have been developed using this parameter^{43,57,58}. Here, we find $T_c/\omega_{\text{ln}} = 0.2$ which is much stronger coupling than the famous "bad actors" Pb and Hg, and is more typical of Pb-Bi alloys. The Errea spectrum gives a similar value of $T_c/\omega_{\text{ln}} = 0.18$. The simple formulas for the famous BCS ratios which are based on this parameter begin to break down by this value. Indeed, another recent calculation³⁰ found a spectrum with a value of 0.3. This is quite extreme for conventional superconductors and only amorphous Bi is listed as having this value. These authors used the simple formulas for calculating the ratios but in this regime the full numerical theory can give quite significant deviations⁴³. We have calculated the three classic BCS ratios for the energy gap $2\Delta_0/k_B T_c$, the specific heat jump at the phase transition $\Delta C(T_c)/\gamma T_c$ with γ , the Sommerfeld constant, and the thermodynamic critical field H_c at zero temperature $\gamma T_c^2/H_c^2(0)$, using the full Eliashberg equations which includes numerical analytic continuation from the imaginary axis equation results to the real axis in order to determine the energy gap Δ_0 . These ratios are listed in Table 1 and we also provide the classic plots of these ratios versus T_c/ω_{ln} , which are shown in Fig. 6. The dashed curves are the simple analytic formulas which were derived as a functional form from Eliashberg theory and then had the coefficients fitted to the numerical and the experimental data in existence at the time. The fits are best at low T_c/ω_{ln} . We have also included data from many conventional superconductors taken from Ref. ⁴³, some of which are labeled. In the limit of $T_c/\omega_{\text{ln}} \rightarrow 0$, the BCS values are recovered. Aluminum is a classic weak coupling BCS superconductor and Pb is a well-studied example of a strong coupling superconductor. The blue stars are from a prior calculation by one of us⁵⁶ for H_3S , where both harmonic^{16,59} and anharmonic¹⁶ phonon spectra were used. The red stars are for our spectrum and the Errea spectrum for LaH_{10} . One sees that even at this value of T_c/ω_{ln} there are deviations from the approximate formula, but nonetheless, LaH_{10} is still within the realm of conventional s-wave, electron-phonon-mediated superconductivity. The deviations between the harmonic versus the anharmonic spectrum reflect that the anharmonic one has the hydrogen phonons pushed to slightly higher ω which increases ω_{ln} .

C. Optical Properties

We now turn to a discussion of optical properties. The reason for focusing on this quantity is twofold. Firstly, the hydrides are in diamond anvil cells under high pressure and this limits the type of experiments which can be performed on these new materials in order to verify

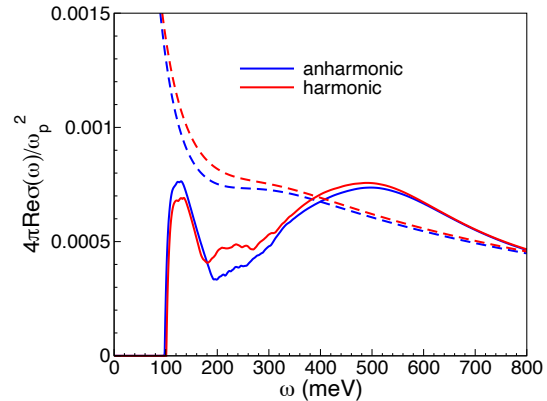


FIG. 7. The real part of the conductivity $4\pi\text{Re}\sigma(\omega)/\omega_P^2$ as a function of photon energy ω . The solid curves are for low temperature $T = 0.1T_c$ and the dashed curves are for $T = T_c$.

theories about them. It has already been shown that optical experiments can be successfully performed on these materials as was done for H_3S ³². Secondly, the optical response is a spectroscopy and this can provide essential information about the superconducting state. Indeed at low photon energy, one can measure the energy gap and, at higher photon energy, one can derive information on the electron-phonon interaction and confirm coupling to high energy bosons. Moreover, a recent proposal³³ demonstrates a method to provide an independent measure of T_c at high photon energy.

In Fig. 7, we show the absorptive part of the conductivity $4\pi\text{Re}\sigma(\omega)/\omega_P^2$ as a function of photon energy ω . Here, ω_P is the plasma frequency. Curves are shown for the low temperature $T/T_c = 0.1$ (solid curves) and the normal state at T_c (dashed curves). A comparison has

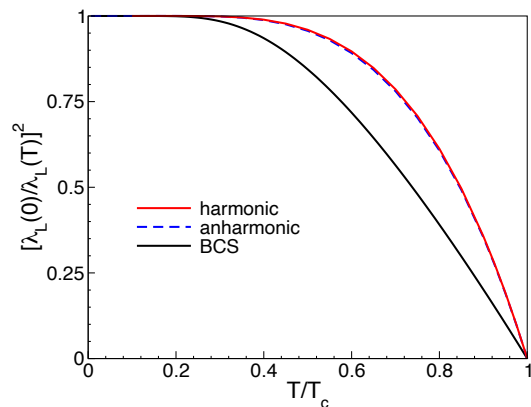


FIG. 8. Superfluid density or the square of the inverse penetration depth $\lambda_L(T)$ versus T/T_c . The two LaH_{10} spectra show classic strong coupling effects beyond the BCS curve but otherwise are virtually the same.

been made between the harmonic and anharmonic spectra, red and blue curves, respectively, and there is very little difference. We have assumed an elastic impurity scattering rate of 100 meV. The opening of an energy gap in the superconducting state manifests itself as zero absorption up until $2\Delta_0 \sim 100$ meV at which point the conductivity rises sharply due to impurity scattering in the system. This region of zero absorption can be used to measure the energy gap⁶⁰. The dip in the absorption reflects structure which can be traced back to energy dependence of the $\alpha^2F(\omega)$ spectrum shifted by $2\Delta_0$. Such structure can be used to extract the $\alpha^2F(\omega)$ ⁶¹. The fact that the main difference between the harmonic and anharmonic spectra occurs in this region illustrates this point as this is the only place where the slightly different energy dependence of the two spectra would manifest. The inelastic scattering due to the electron-phonon interaction gives rise to a large bump in the conductivity which overshoots the normal state, primarily reflecting a shift in such structure with the opening an energy gap upon going from the normal to the superconducting state^{33,62}. The stronger variations in the superconducting state over the normal state is a reflection of the square root singularity in the superconducting quasiparticle density of states which enters the evaluation of the conductivity^{44,45,47}. The loss in spectral weight at low energy is found in the superconducting condensate and is represented by the superfluid density shown in Fig. 7 (related to the inverse square of the penetration depth $\lambda_L(T)$). Here we find that the superfluid density shows the classic temperature dependence of a strong-coupling superconductor where the curve is higher than the BCS one. Both anharmonic and harmonic spectra give essentially the same result here. The penetration depth can be measured from the optical response via the imaginary part of the conductivity for $\omega \rightarrow 0$. Note that the imaginary part of σ is related to the real part via Kramers-Kronig relations. Finally, returning to the real part of the conductivity in Fig. 7, the bump up at high energy here is quite large and its temperature dependence can be used to measure the T_c because the bump will reduce and shift to lower ω as the energy gap closes with increasing T , while the normal state conductivity will increase in width with temperature.

To best understand this last point, we move to the reflectance. While both the complex conductivity and the related complex reflectance can be calculated theoretically and measured via experiment, it is the reflectance that is the directly measured quantity. The phase of the reflectance must be obtained through Kramers-Kronig but once this is known, there are simple formulas that provide the connection to the real and imaginary parts of σ through the complex dielectric function. In Fig. 9, we show the reflectance that we have calculated for our spectrum at a large number of temperatures from close $0.1T_c$ to $0.995T_c$, using $\omega_P = 31$ eV and correcting for the diamond refractive index. The perfect reflection at low temperature and frequencies up to 100 meV iden-

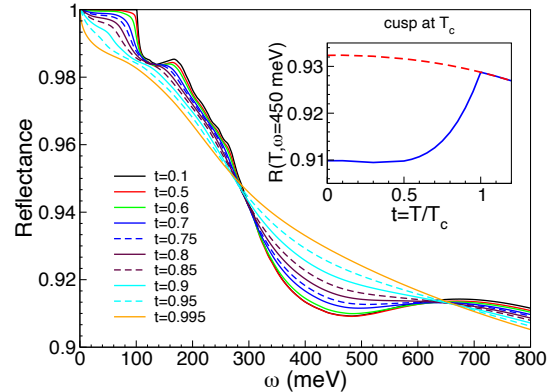


FIG. 9. Reflectance versus ω for various temperatures $t = T/T_c$ in the superconducting state. The inset shows the reflectance as a function of temperature for a fixed photon energy of 450 meV. The blue curve below T_c is the superconducting state and the red dashed curve is the normal state result that would be measured in the absence of superconductivity.

tifies the energy gap $2\Delta_0$. The strong variation in the region of 300-600 meV is where the temperature dependence is moving upwards whereas in the normal state it would move downwards. If we fix at a particular photon energy (in this case 450 meV) and plot the reflectance as a function of temperature, we have the blue curve shown in the inset, which shows a cusp at T_c as the temperature dependence changes behavior from the superconducting state to the normal state. The red dashed curve is that for the normal state shown down to zero temperature, if superconductivity is suppressed. This cusp feature in the reflectance at fixed ω can be used as an additional non-contact method to determine T_c ³³. Moreover, as these materials are in a diamond anvil cell in order to be at high pressure, optical measurements are one of the few probes available under these conditions and this range of photon energy is above that where there would be a strong obscuring response due to the diamond in the pressure cell. This has yet to be tested but successful optical measurements in this energy range were performed on pressurized H_3S to confirm coupling to a high energy boson for superconductivity³² and so we are confident that this experiment is possible and estimates indicate that it should be.

IV. CONCLUSIONS

In summary, we have used a combination of first-principle DFT calculations and Migdal-Eliashberg theory to study the mechanism of superconductivity in LaH_{10} , which has the highest known T_c . We have demonstrated that the large T_c is driven by the coupling of the electrons to hydrogen phonons and that the La contribution to T_c

is small. We have provided a thorough discussion of the nature of T_c , resulting from a mechanism which is highly optimized in this material, and have shown where LaH₁₀ sits in relation to conventional electron-phonon superconductors in terms of strong coupling parameters and the classic BCS ratios. Finally, we have highlighted the optical properties, in particular, as a means to determine the energy gap, the superconducting mechanism, and independently confirm T_c . Measurement of optical properties on pressurized H₃S has demonstrated the potential for success of this technique and its ability to confirm our predictions.

ACKNOWLEDGMENTS

S.F.E thanks Ion Errea, Roald Hoffmann, and Stanimir Bonev for useful discussions. E.J.N. and T.T.

acknowledge the late J.P. Carbotte for important discussions and contributions on this topic. In addition, we also thank M.I. Erements for ongoing collaborations and discussions related to LaH₁₀. We also thank H. Liu and R.J. Hemley for providing their $\alpha^2F(\omega)$ from Ref. 25, although it has not been used here. This work was funded by Natural Sciences and Engineering Research Council of Canada (NSERC) (EJN,TT). This research was enabled in part by support provided by Graham & Cedar and Compute Canada (www.computecanada.ca).

-
- * Electronic address: sabri.elatresh@dal.ca, enicol@uoguelph.ca
- ¹ N. W. Ashcroft, Phys. Rev. Lett. **21**, 1748 (1968), URL <https://link.aps.org/doi/10.1103/PhysRevLett.21.1748>.
 - ² H. K. Mao and R. J. Hemley, Science **244**, 1462 (1989).
 - ³ M. I. Erements and I. A. Troyan, Nat. Mater. **10**, 927 (2011).
 - ⁴ R. P. Dias and I. F. Silvera, Science **355**, 715 (2017), ISSN 0036-8075, URL <https://science.sciencemag.org/content/355/6326/715>.
 - ⁵ P. Loubeyre, F. Occelli, and P. Dumas, Nature **577**, 631 (2020).
 - ⁶ J. A. Flores-Livas, L. Boeri, A. Sanna, G. Profeta, R. Arita, and M. Erements, *A perspective on conventional high-temperature superconductors at high pressure: Methods and materials* (2019), 1905.06693.
 - ⁷ L. Zhang, Y. Wang, J. Lv, and Y. Ma, Nature Reviews Materials **2**, 17005 (2017), ISSN 2058-8437, URL <https://doi.org/10.1038/natrevmats.2017.5>.
 - ⁸ A. R. Oganov, C. J. Pickard, Q. Zhu, and R. J. Needs, Nature Reviews Materials **4**, 331 (2019), ISSN 2058-8437, URL <https://doi.org/10.1038/s41578-019-0101-8>.
 - ⁹ C. J. Pickard, I. Errea, and M. I. Erements, Annu. Rev. Condens. Matter Phys. **11**, 57 (2020).
 - ¹⁰ Y. Li, L. Wang, H. Liu, Y. Zhang, J. Hao, C. J. Pickard, J. R. Nelson, R. J. Needs, W. Li, Y. Huang, et al., Phys. Rev. B **93**, 020103 (2016), URL <http://link.aps.org/doi/10.1103/PhysRevB.93.020103>.
 - ¹¹ T. A. Strobel, P. Ganesh, M. Somayazulu, P. R. C. Kent, and R. J. Hemley, Phys. Rev. Lett. **107**, 255503 (2011), URL <http://link.aps.org/doi/10.1103/PhysRevLett.107.255503>.
 - ¹² Y. Li, J. Hao, H. Liu, Y. Li, and Y. Ma, The Journal of Chemical Physics **140**, 174712 (2014), <http://dx.doi.org/10.1063/1.4874158>, URL <http://dx.doi.org/10.1063/1.4874158>.
 - ¹³ D. Duan, Y. Liu, F. Tian, D. Li, X. Huang, Z. Zhao, H. Yu, B. Liu, W. Tian, and T. Cui, Scientific Reports **4**, 6968 (2014), ISSN 2045-2322, URL <https://doi.org/10.1038/srep06968>.
 - ¹⁴ A. P. Drozdov, M. I. Erements, I. A. Troyan, V. Ksenofontov, and S. I. Shylin, Nature **525**, 73 (2015), ISSN 0028-0836, letter, URL <http://dx.doi.org/10.1038/nature14964>.
 - ¹⁵ D. Duan, X. Huang, F. Tian, D. Li, H. Yu, Y. Liu, Y. Ma, B. Liu, and T. Cui, Phys. Rev. B **91**, 180502 (2015), URL <http://link.aps.org/doi/10.1103/PhysRevB.91.180502>.
 - ¹⁶ I. Errea, M. Calandra, C. J. Pickard, J. Nelson, R. J. Needs, Y. Li, H. Liu, Y. Zhang, Y. Ma, and F. Mauri, Phys. Rev. Lett. **114**, 157004 (2015), URL <http://link.aps.org/doi/10.1103/PhysRevLett.114.157004>.
 - ¹⁷ N. Bernstein, C. S. Hellberg, M. D. Johannes, I. I. Mazin, and M. J. Mehl, Phys. Rev. B **91**, 060511 (2015), URL <http://link.aps.org/doi/10.1103/PhysRevB.91.060511>.
 - ¹⁸ I. Errea, M. Calandra, C. J. Pickard, J. R. Nelson, R. J. Needs, Y. Li, H. Liu, Y. Zhang, Y. Ma, and F. Mauri, Nature **532**, 81 (2016), ISSN 0028-0836, letter, URL <http://dx.doi.org/10.1038/nature17175>.
 - ¹⁹ M. Einaga, M. Sakata, T. Ishikawa, K. Shimizu, M. I. Erements, A. P. Drozdov, I. A. Troyan, N. Hirao, and Y. Ohishi, Nat Phys **12**, 835 (2016), ISSN 1745-2473, letter, URL <http://dx.doi.org/10.1038/nphys3760>.
 - ²⁰ B. Guigue, A. Marizy, and P. Loubeyre, Phys. Rev. B **95**, 020104 (2017), URL <http://link.aps.org/doi/10.1103/PhysRevB.95.020104>.
 - ²¹ A. F. Goncharov, S. S. Lobanov, I. Kruglov, X.-M. Zhao, X.-J. Chen, A. R. Oganov, Z. Konôpková, and V. B. Prakapenka, Phys. Rev. B **93**, 174105 (2016), URL <http://link.aps.org/doi/10.1103/PhysRevB.93.174105>.
 - ²² X. Feng, J. Zhang, G. Gao, H. Liu, and H. Wang, RSC Adv. **5**, 59292 (2015), URL <http://dx.doi.org/10.1039/C5RA11459D>.
 - ²³ H. Wang, J. S. Tse, K. Tanaka, T. Iitaka, and Y. Ma, Proceedings of the National Academy of Sciences **109**, 6463 (2012), ISSN 0027-8424, <https://www.pnas.org/content/109/17/6463.full.pdf>,

- URL <https://www.pnas.org/content/109/17/6463>.
- ²⁴ Y. Li, J. Hao, H. Liu, J. S. Tse, Y. Wang, and Y. Ma, *Scientific Reports* **5**, 9948 (2015), ISSN 2045-2322, URL <https://doi.org/10.1038/srep09948>.
- ²⁵ H. Liu, I. I. Naumov, R. Hoffmann, N. W. Ashcroft, and R. J. Hemley, *Proceedings of the National Academy of Sciences* **114**, 6990 (2017), ISSN 0027-8424, <https://www.pnas.org/content/114/27/6990.full.pdf>, URL <https://www.pnas.org/content/114/27/6990>.
- ²⁶ F. Peng, Y. Sun, C. J. Pickard, R. J. Needs, Q. Wu, and Y. Ma, *Phys. Rev. Lett.* **119**, 107001 (2017), URL <https://link.aps.org/doi/10.1103/PhysRevLett.119.107001>.
- ²⁷ Z. M. Geballe, H. Liu, A. K. Mishra, M. Ahart, M. Somayazulu, Y. Meng, M. Baldini, and R. J. Hemley, *Angewandte Chemie International Edition* **57**, 688 (2018), URL <https://onlinelibrary.wiley.com/doi/abs/10.1002/anie.201709970>.
- ²⁸ M. Somayazulu, M. Ahart, A. K. Mishra, Z. M. Geballe, M. Baldini, Y. Meng, V. V. Struzhkin, and R. J. Hemley, *Phys. Rev. Lett.* **122**, 027001 (2019), URL <https://link.aps.org/doi/10.1103/PhysRevLett.122.027001>.
- ²⁹ A. P. Drozdov, P. P. Kong, V. S. Minkov, S. P. Besedin, M. A. Kuzovnikov, S. Mozaffari, L. Balicas, F. F. Balakirev, D. E. Graf, V. B. Prakapenka, et al., *Nature* **569**, 528 (2019), ISSN 1476-4687, URL <https://doi.org/10.1038/s41586-019-1201-8>.
- ³⁰ I. A. Kruglov, D. V. Semenok, H. Song, R. Szczesniak, I. A. Wrona, R. Akashi, M. M. Davari Esfahani, D. Duan, T. Cui, A. G. Kvashnin, et al., *Phys. Rev. B* **101**, 024508 (2020), URL <https://link.aps.org/doi/10.1103/PhysRevB.101.024508>.
- ³¹ I. Errea, F. Belli, L. Monacelli, A. Sanna, T. Koretsune, T. Tadano, R. Bianco, M. Calandra, R. Arita, F. Mauri, et al., *Nature* **578**, 66 (2020), ISSN 1476-4687, URL <https://doi.org/10.1038/s41586-020-1955-z>.
- ³² F. Capitani, B. Langerome, J.-B. Brubach, P. Roy, A. Drozdov, M. I. Erements, E. J. Nicol, J. P. Carbotte, and T. Timusk, *Nature Physics* **13**, 859 (2017), ISSN 1745-2481, URL <https://doi.org/10.1038/nphys4156>.
- ³³ J. P. Carbotte, E. J. Nicol, and T. Timusk, *Phys. Rev. Lett.* **121**, 047002 (2018), URL <https://link.aps.org/doi/10.1103/PhysRevLett.121.047002>.
- ³⁴ X. Gonze, B. Amadon, P.-M. Anglade, J.-M. Beuken, F. Bottin, P. Boulanger, F. Bruneval, D. Caliste, R. Caracas, et al., *Computer Physics Communications* **180**, 2582 (2009), ISSN 0010-4655, URL <http://www.sciencedirect.com/science/article/pii/S0010465509002276>.
- ³⁵ C. Hartwigsen, S. Goedecker, and J. Hutter, *Phys. Rev. B* **58**, 3641 (1998), URL <https://link.aps.org/doi/10.1103/PhysRevB.58.3641>.
- ³⁶ S. Goedecker, M. Teter, and J. Hutter, *Phys. Rev. B* **54**, 1703 (1996), URL <https://link.aps.org/doi/10.1103/PhysRevB.54.1703>.
- ³⁷ See Supplemental Material at <http://link.aps.org/supplemental/xxx/PhysRevB.xx.xxxx>, for structural information, DOS, phonon density, and distances analysis.
- ³⁸ C. Wang, S. Yi, and J.-H. Cho, *Phys. Rev. B* **101**, 104506 (2020), URL <https://link.aps.org/doi/10.1103/PhysRevB.101.104506>.
- ³⁹ X. Gonze, *Phys. Rev. B* **55**, 10337 (1997), URL <https://link.aps.org/doi/10.1103/PhysRevB.55.10337>.
- ⁴⁰ A. Y. Liu and A. A. Quong, *Phys. Rev. B* **53**, R7575 (1996), URL <https://link.aps.org/doi/10.1103/PhysRevB.53.R7575>.
- ⁴¹ S. Y. Savrasov and D. Y. Savrasov, *Phys. Rev. B* **54**, 16487 (1996), URL <https://link.aps.org/doi/10.1103/PhysRevB.54.16487>.
- ⁴² R. Bianco, I. Errea, M. Calandra, and F. Mauri, *Phys. Rev. B* **97**, 214101 (2018), URL <https://link.aps.org/doi/10.1103/PhysRevB.97.214101>.
- ⁴³ J. P. Carbotte, *Rev. Mod. Phys.* **62**, 1027 (1990), URL <https://link.aps.org/doi/10.1103/RevModPhys.62.1027>.
- ⁴⁴ F. Marsiglio and J. P. Carbotte, in *Superconductivity in Conventional and Unconventional Superconductors*, edited by K. Bennemann and J. Ketterson (Springer, Berlin, 2008), pp. 73–162.
- ⁴⁵ J. P. Carbotte, E. J. Nicol, and T. Timusk, *Phys. Rev. B* **100**, 094505 (2019), URL <https://link.aps.org/doi/10.1103/PhysRevB.100.094505>.
- ⁴⁶ F. Marsiglio, M. Schossmann, and J. P. Carbotte, *Phys. Rev. B* **37**, 4965 (1988), URL <https://link.aps.org/doi/10.1103/PhysRevB.37.4965>.
- ⁴⁷ R. Akis, J. P. Carbotte, and T. Timusk, *Phys. Rev. B* **43**, 12804 (1991), URL <https://link.aps.org/doi/10.1103/PhysRevB.43.12804>.
- ⁴⁸ Y. Quan, S. S. Ghosh, and W. E. Pickett, *Phys. Rev. B* **100**, 184505 (2019), URL <https://link.aps.org/doi/10.1103/PhysRevB.100.184505>.
- ⁴⁹ D. A. Papaconstantopoulos, M. J. Mehl, and P.-H. Chang, *Phys. Rev. B* **101**, 060506 (2020), URL <https://link.aps.org/doi/10.1103/PhysRevB.101.060506>.
- ⁵⁰ D. Rainer and F. J. Culetto, *Phys. Rev. B* **19**, 2540 (1979), URL <https://link.aps.org/doi/10.1103/PhysRevB.19.2540>.
- ⁵¹ A. P. Durajski, R. Szczesniak, Y. Li, C. Wang, and J.-H. Cho, *Isotope effect in superconducting lanthanum hydride under high compression* (2019), arXiv:1912.09663.
- ⁵² W. L. McMillan, *Phys. Rev.* **167**, 331 (1968), URL <https://link.aps.org/doi/10.1103/PhysRev.167.331>.
- ⁵³ P. B. Allen and R. C. Dynes, *Phys. Rev. B* **12**, 905 (1975), URL <https://link.aps.org/doi/10.1103/PhysRevB.12.905>.
- ⁵⁴ C. R. Leavens, *Solid State Commun.* **17**, 1499 (1975).
- ⁵⁵ C. R. Leavens and J. P. Carbotte, *J. Low Temp. Phys.* **14**, 195 (1974).
- ⁵⁶ E. J. Nicol and J. P. Carbotte, *Phys. Rev. B* **91**, 220507 (2015), URL <https://link.aps.org/doi/10.1103/PhysRevB.91.220507>.
- ⁵⁷ B. Mitrovic, H. G. Zarate, and J. P. Carbotte, *Phys. Rev. B* **29**, 184 (1984), URL <https://link.aps.org/doi/10.1103/PhysRevB.29.184>.
- ⁵⁸ F. Marsiglio and J. P. Carbotte, *Phys. Rev. B* **33**, 6141 (1986), URL <https://link.aps.org/doi/10.1103/PhysRevB.33.6141>.
- ⁵⁹ J. A. Flores-Livas, A. Sanna, and E. K. U. Gross, *Euro. Phys. J. B* **89**, 63 (2016).
- ⁶⁰ T. Mori, E. J. Nicol, S. Shiizuka, K. Kuniyasu, T. Noji ma, N. Toyota, and J. P. Carbotte, *Phys. Rev. B* **77**, 174515 (2008), URL <https://link.aps.org/doi/10.1103/PhysRevB.77.174515>.
- ⁶¹ B. Farnworth and T. Timusk, *Phys. Rev. B* **14**, 5119 (1976), URL <https://link.aps.org/doi/10.1103/PhysRevB.14.5119>.
- ⁶² P. B. Allen, *Phys. Rev. B* **3**, 305 (1971).